# NUMERICAL PREDICTIONS OF WING-TIP EFFECTS ON LIFT-INDUCED DRAG

**P. Bourdin**
**ONERA - Applied Aerodynamics Department**
**BP72, 92322 Châtillon Cedex, France**

**Keywords:** *far field analysis, lift-induced drag reduction, wing-tip dihedral*

## Abstract

*This paper points out two small effects concerning lift-induced drag and wing-tip dihedral. To this end, a far field technique is used to extract drag from Euler computations. Numerical predictions show that at fixed projected span downward winglets produce less lift-induced drag than upward winglets of the same length. It is also found that at fixed winglet length, the minimum lift-induced drag is obtained with a little negative dihedral. These two effects are thought to be due to a better layout of the bound vorticity relative to the trailing vorticity.*

## Nomenclature

| | |
|---|---|
| $\delta$ | dihedral angle |
| $\gamma$ | specific heat ratio |
| $\rho$ | air density |
| $\Gamma$ | circulation |
| $\Lambda$ | aspect ratio |
| $h_i$ | specific stagnation enthalpy |
| $\vec{q}$ | local velocity vector |
| $r_a$ | air specific constant |
| $s$ | specific entropy |
| $u, v, w$ | $x, y, z$ wind-axis velocity components |
| $C_{D_i}$ | lift-induced drag coefficient |
| $C_L$ | lift coefficient |
| $D_i$ | lift-induced drag |
| $D_{v+w}$ | irreversible drag (viscous + wave) |
| $M$ | Mach number |
| $X_\infty$ | freestream value of $X$ |
| $\Delta X$ | $X - X_\infty$ |



## 1 Introduction

Lift-induced drag minimization has been a subject of interest since Prandtl[7] developed his lifting line theory. In the frame of this theory, the planar wing with spanwise elliptic loading was proven to produce less lift-induced drag than any other planar wing with the same span and lift. The minimum lift-induced drag of non-planar wing shapes was addressed by Munk[6], and analytical solutions for certain non-planar lifting systems were derived by Cone[1]. Thus, the problem has been well outlined from a theoretical point of view. More recently with the advent of super-computers, numerical methods based on more complete flow models than those of Prandtl or Munk have been used to address the problem [16][10]. In light of the obtained numerical results, two points must be emphasized. First point, only small effects seem to be found out when comparing the predicted results to the results of the linear theory of Prandtl and Munk. Second point, since small effects are expected, numerical methods allowing sufficient accuracy must be used.

The present paper is intended to highlight some small effects in lift-induced drag reduction by providing accurate results coming from the post-processing of Euler numerical flow so-

lutions, and to compare them to results obtained in the frame of linear theory, as well as to results obtained in the frame of a recent mathematical model derived by Eppler[4].

## 2 Numerical Approach

### 2.1 Mathematical Model

The wide use of inviscid flow equations for studying lift-induced drag, rather than more complete models of the flow accounting for viscosity, is based on the physical concept that the mechanism for producing lift-induced drag is the influence of the wing trailing vortex sheet on the wing itself, a fundamentally inviscid mechanism[10]. Although viscosity is required to produce a circulation distribution along the wing span, the magnitude of this circulation and the associated wake vorticity are essentially independent on the fluid viscosity as long as no separation occurs.

By ascending order of modelisation level, the available numerical methods for solving inviscid flows are:

1. vortex lattice methods (VLM)
2. panel methods
3. full-potential CFD codes
4. Euler CFD codes

Methods of classes $1-3$ have a much lower computational cost than methods of class $4$. This is why they are still often preferred to Euler codes for lift-induced drag parametric studies. Their main weakness lies in the wake model, because they all require that the wake geometry be specified or fitted as a boundary condition before the numerical solution takes place. On the contrary, the freely deforming wake shape is captured in the solution with Euler codes. Therefore, an Euler code will be mainly used in this paper, as it gives the most complete description of an inviscid flow. However, Euler numerical flow solutions show some spurious viscous-like behavior, which makes surface pressure integration quite inaccurate for drag prediction[8][12]. An issue is provided by the use of the momentum theorem, which relates drag to a surface integral in the so-called Trefftz plane (a plane far downstream of the lifting surface and normal to the freestream direction). This approach is called the far field approach, and in the case of inviscid subsonic flows, the Trefftz-plane integral corresponds to lift-induced drag only. Numerical results obtained with this technique are found to be much more accurate than those obtained by surface pressure integration[8]. Thus, an Euler code combined with a far field analysis can offer the adequate precision to highlight small effects in lift-induced drag reduction.

### 2.2 Computational Sequence

#### *2.2.1 Flow Solver*

The ONERA Euler solver CANARI[15] is used to simulate steady inviscid compressible flows around 3D configurations. The code uses a finite volume method based on a cell-centered approach and structured multi-block grids. Jameson's second order central scheme is applied for spatial discretization[5] and a four stage Runge-Kutta explicit method is taken as a time marching approach. In order to suppress spurious oscillations and overshoots near flow discontinuities and stagnation points, blended second and fourth difference non-linear artificial dissipation terms are added to the governing discretized equations.

#### *2.2.2 Post-Processor for Drag Extraction*

Drag is extracted through a field analysis. This technique, which requires a complex post-processing of the numerical flow solution, gives a phenomenological breakdown into physical components (lift-induced drag, wave drag, and with the Navier-Stokes equations, viscous drag). Besides, numerical schemes and meshes used in CFD produce spurious drag sources which may be distinguished from physical drag, and eliminated, by an appropriate analysis of the field. This is the main asset of the far field technique, since spurious contributions to drag

cannot be distinguished from physical production by surface force integration[3][8] (spurious contributions are embedded in the pressure and shear stress distributions over the body skin). The field analysis method developed at ONERA is a post-processor to Euler and Navier-Stokes solutions computed with multi-block structured grids.

The theoretical basis of far field drag derivation is the use of the momentum theorem. In the case of Euler or Navier-Stokes flow models, its straight application yields only the total drag and does not allow physical components to be extracted. However, wave and viscous drag (the latter in the Navier-Stokes model) are produced by irreversible phenomena, while lift-induced drag is related to reversible phenomena through which transverse kinetic energy is added to the flow downstream of lifting finite surfaces. Then, through an appropriate choice of variables, numerical approximations and phenomenological considerations, expressions for irreversible drag and lift-induced drag can be derived from the momentum theorem. The formulation used in the ONERA method follows van der Vooren's reference[13]: let $\mathcal{V}_0$ denote the volume inside a closed surface containing the aircraft, the shock waves, and the areas dominated by the effects of viscosity. Then the drag force produced by irreversible phenomena can be expressed as:

$$D_{v+w} = \iiint_{\mathcal{V}_0} div\, \vec{f}_{v+w}\, d\vartheta \qquad (1)$$

with

$$\vec{f}_{v+w} = -\rho\, q_\infty \left( \sqrt{1 + \frac{2\Delta h_i}{q_\infty^2} - 2\,\frac{e^{\left(\frac{\gamma-1}{\gamma}\right)\frac{\Delta s}{r_a}} - 1}{(\gamma-1)M_\infty^2}} - 1 \right) \vec{q} \qquad (2)$$

The lift-induced drag, computed on a transverse surface $\mathcal{S}_\mathcal{T}$ large enough for flow perturbations to vanish on its outer boundary, and far enough downstream from the lifting system for longitudinal gradients to be negligible, is given by:

$$D_i = \iint_{\mathcal{S}_\mathcal{T}} \vec{f}_i . \vec{n}\, d\sigma \qquad (3)$$

with

$$\vec{f}_i = \frac{\rho_\infty}{2} \begin{pmatrix} v^2 + w^2 - (1 - M_\infty^2)\Delta u^{\star 2} \\ -2\,\Delta u^\star\, v \\ -2\,\Delta u^\star\, w \end{pmatrix} \qquad (4)$$

where the vector coordinates are given in the aerodynamic frame, and

$$\Delta u^\star = u - q_\infty + q_\infty \left( \frac{1}{\gamma M_\infty^2}\,\frac{\Delta s}{r_a} - \frac{\Delta h_i}{q_\infty^2} \right) \qquad (5)$$

An original feature of the ONERA method concerns lift-induced drag prediction which is of main interest in this paper. It has been observed that in numerical solutions of lifting flow problems, the transverse kinetic energy decreases downstream of the body at a much faster rate than in reality[2]. Actually, with the Euler theoretical model, it should not decrease at all when assuming incompressible flows. This phenomenon has been ascribed to the effect of artificial dissipation which can be strong in the far field, grids becoming unavoidably very coarse in this area. Unfortunately, this transverse kinetic energy appears in the formula given previously for $D_i$, and is the term which becomes dominant far enough downstream from the lifting system. Therefore lift-induced drag directly computed with this formula (see Eq. 3 to 5) decreases as the integration surface moves downstream. An example of the evolution of the quantity, which will henceforth be called "apparent lift-induced drag" rather than lift-induced drag, is presented in Fig. 1. Part of the lift-induced drag is in fact transformed into spurious viscous drag, mostly in the area of the tip vortex. This being like an irreversible phenomenon, the resulting spurious drag can be computed by applying the formula for irreversible drag (see Eq. 1 and 2) between the origin of the tip vortex and $\mathcal{S}_\mathcal{T}$, the surface of integration of the apparent lift-induced drag. The correction thus computed (automatically) by the ONERA method matches the loss of apparent lift-induced drag, and if added to this quantity, gives results almost independent of the location of $\mathcal{S}_\mathcal{T}$ (see Fig. 1), as it must be in the Euler theoretical model for subcritical flows.

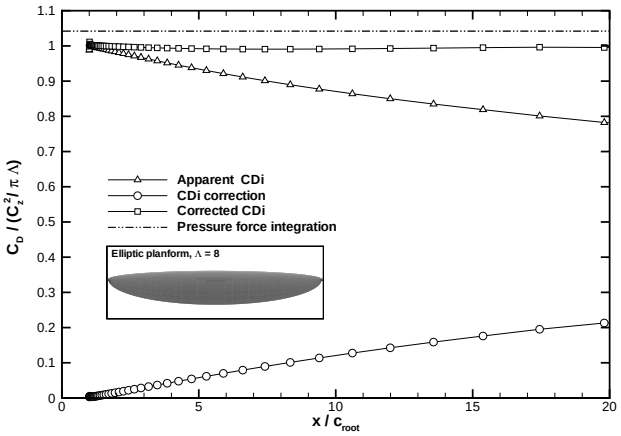


**Fig. 1** Exhaustive far field drag analysis in inviscid 3D flow (Euler computation, $M_\infty = 0.2$).

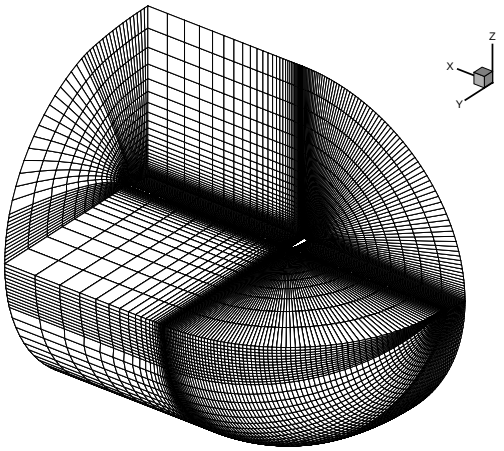

**Fig. 2** Cut-away isometric view of the 3D computational grid (fine clustering of points around the wing edges and aft of the trailing edge to better capture pressure and velocity gradients).

### *2.2.3 Computational Test Case*

An untwisted wing of elliptic planform ($\Lambda = 8$, NACA 0012 airfoil) is considered in a low-speed inviscid flow ($M_\infty = 0.2$) at an 8-degree angle of attack. Therefore, wave and viscous drag components do not exist, and only lift-induced drag remains. According to the Prandtl lifting line theory, the lift-induced drag coefficient should be equal to $\frac{C_L^2}{\pi\Lambda}$ for this planform.

Due to the flow symmetry, only the semi-span of the wing is modeled. A slight adaptation of the tip (rounded wing-tip) has been used to facilitate the grid generation. A cut-away isometric view of the wing and the 3D computational grid is shown in Fig. 2. The Euler numerical flow solution is obtained with standard values for the artificial dissipation coefficients ($0.25$ for the 2nd difference coefficient, and $0.016$ for the 4th difference coefficient). The results of the field analysis for this test case are summarized in Fig. 1. It can be seen that the corrected lift-induced drag value is very close to $\frac{C_L^2}{\pi\Lambda}$ all along the downstream part of the computational domain. On the contrary, the pressure force integration overestimates this expected result by about $4\%$.

So, a reliable and accurate method to predict lift-induced drag from Euler calculations consists in computing from a transverse survey plane the apparent lift-induced drag, which has to be corrected by using Eq. 1 to evaluate the part of lift-induced drag converted into spurious drag between the trailing edge and the survey plane.

## 3 Parametric Study of the Wing-Tip Dihedral Effects

In a recent paper by Eppler[4], a new mathematical model has been established that allows one special nonlinear effect related to lift-induced drag, the induced lift, to be evaluated. Induced lift is caused by the velocity which the bound vortices (i.e. the vortices that model the lifting system) induce on themselves and does not develop on a straight planar wing. When induced lift is positive, this effect is similar to reducing the lift-induced drag for a given (total) lift. Under the basic assumption of a rigid wake parallel to the flow at infinity, Eppler evaluated the induced lift of a wing with winglets by means of exact formulas and efficient numerical procedures. Two fundamental results of his study are:

- Winglets up are much better than winglets down in terms of lift-induced drag reduction.
- A winglet with a dihedral of about $10°$ gives a lower lift-induced drag than a planar extension of the same length.

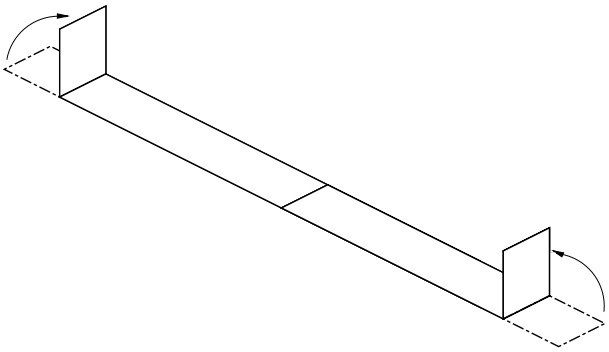

**Fig. 3** Inclination of the wing-tips at fixed deployed span.

The present investigation examines the impact of wing-tip dihedral on the performance of a rectangular planform.

## 3.1 Methodology

The frontal shape of a rectangular planform is incrementally deformed by bending upward or downward its tips within a range from $0$ to $90°$, as sketched in Fig. 3. In this manner, the *deployed* span of the wing remains unchanged, whereas its *projected* span shrinks. *Deployed* span is the length of the curve defining the shape of the wing in front view. *Projected* span is the horizontal distance separating one tip from the other. The performance of the wing with deflected tips is then examined against the baseline planar wing. One advantage resulting from this methodology is that viscous drag may be considered constant too (fixed wetted area) and then benefits in lift-induced drag will also lead to benefits in total drag.

## 3.2 Computational Set-Up

### *3.2.1 Wing Geometry and Grids*

The baseline rectangular wing is lofted with NACA 0012 airfoil sections. It has an aspect ratio of $8$ and $15\%$ of its deployed span is bent up or down. Both untwisted and twisted cases are considered. The computational grids are generated by stacking along the wing span the 2D curvilinear and body-fitted mesh of the wing-root section. Each grid contains about $500\,000$ cells laid in a $C-O$ topology, like in Fig. 2. It extends about 40 chords in the spanwise direction, about 60 in the streamwise direction, and about 60 in the vertical direction (30 from each wing side). The extension behind the trailing edge amounts to 30 chords. Grids for the deflected tips are obtained from the grid of the baseline configuration by rotating the wing-tip boundary by the desired dihedral angle while keeping the outer boundary of the computational domain fixed. Between these two boundaries, the rotation of the mesh nodes is linearly damped by a relaxation factor. Front views are shown in Fig. 4.

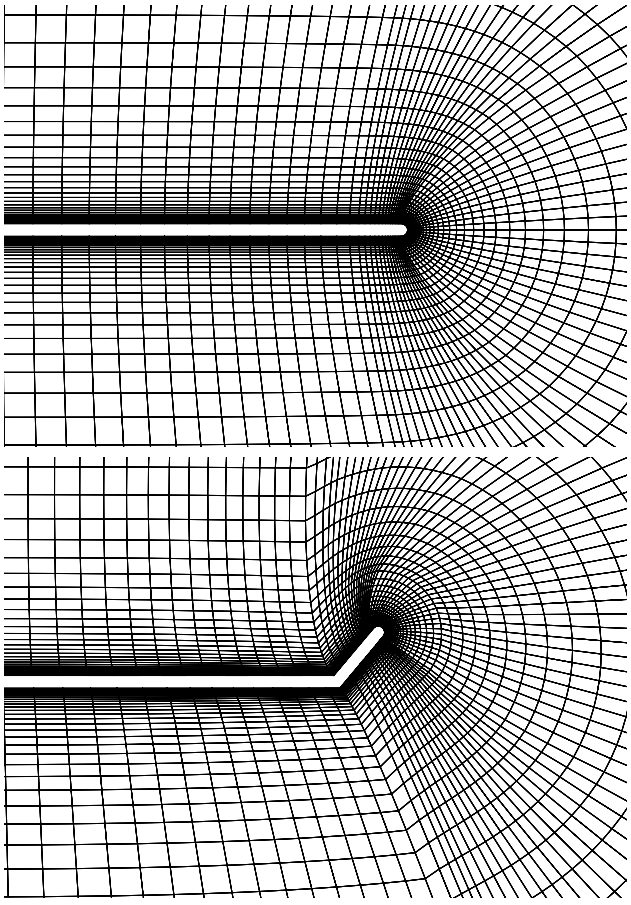

**Fig. 4** Front view of the mesh before (top) and after (bottom) deformation.

### *3.2.2 Computational Parameters*

All the Euler computations presented in this paper are carried out with standard dissipation coefficient values. In order to ensure an accurate

field analysis, the convergence is extended as far as necessary for each calculation.

### *3.2.3 Flow Condition*

The flow condition corresponds to a freestream Mach number of $0.2$. The lift force is the same for all the investigated configurations, and corresponds to a lift coefficient of $0.6$ based on the baseline wing area.

## 3.3 Numerical Results

Configurations are analyzed in terms of relative lift-induced drag, that is the lift-induced drag normalized by the minimum lift-induced drag expected for the baseline planar configuration in classical linear theory. As a first attempt, only untwisted wings are considered. Then, as a second attempt, wings with optimal twist relative to lift-induced drag reduction are examined.

### *3.3.1 Untwisted Configurations*

The relative lift-induced drag predicted from the far field analysis of the Euler numerical flow solution is plotted versus the dihedral angle in Fig. 5. It can be seen that the resulting curve is not symmetric with respect to the sign of the dihedral angle (positive angles correspond to wing-tips up and negative angles to wing-tips down), and as soon as the wing becomes significantly non-planar lift-induced drag increases. The consequences of these features are:

- For a given amount of wing-tip dihedral, wing-tips down produce less lift-induced drag than wing-tips up.
- The minimum of lift-induced drag is obtained with a small negative dihedral angle (about $5°$).

These two items contradict Eppler's results and will be discussed after the next section.

### *3.3.2 Optimally-Twisted Configurations*

In order to check if the previous results would still stand for optimally-loaded wings, a numerical optimization is processed by means of a gradient-based method. Because the spanwise loading over a wing with given sweep and taper ratio is determined by the twist distribution, searching the adequate spanwise loading that minimizes lift-induced drag comes down to searching the twist distribution associated with that optimum. This is done by handling the twist distribution as a 4th order Bezier curve whose control points are the design variables supplied to the gradient-based optimizer CONMIN[14]. To quickly solve for the optimal twist distribution, a VLM featuring one row of 100 spanwise horseshoe vortices (i.e. a discrete vortex Weissinger model) is used as the aerodynamic solver coupled with CONMIN. The resulting optimal twist distribution is then checked against the Euler solver. In the case of the optimally-twisted planar configuration, the far-field drag predicted from the Euler numerical solution is very close to the theoretical value derived in the frame of the lifting-line theory. Indeed, we obtain a relative lift-induced drag of $0.998$ with this configuration. The rest of the Euler far field drag results are plotted versus the dihedral angle in Fig. 5. There is still an asymmetry in favor of downward wing-tips, and a minimum around $-5°$.

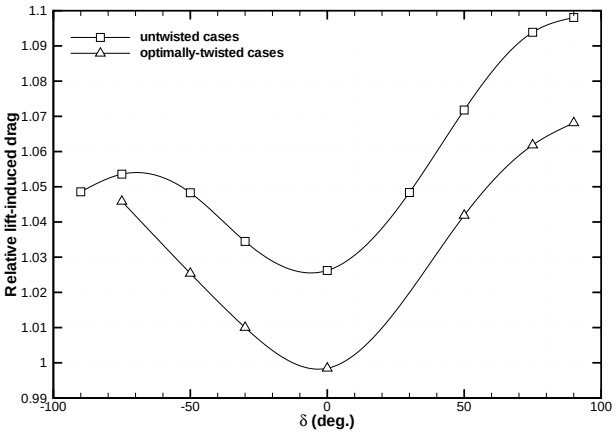


**Fig. 5** Relative lift-induced drag of the investigated configurations (twisted and untwisted cases).

### 3.4 Discussion

In linear theory, optimized downward and upward winglets of the same height produce the same performance because it is the cosine of the dihedral angle that appears in the governing equations for minimum lift-induced drag. In Eppler's model, induced lift (neglected in linear theory) disrupts this symmetry and upward winglets are then favored. On the contrary in the present study which involves far field analysis of Euler numerical flow solutions, winglets are predicted more efficient when bent down regardless they are optimized or not.

First, let us consider the Euler far field results against the linear theory. The discrepancy between them may be explained as follows[9]. The lift and drag forces as calculated in the frame of the linear theory are completely independent of the way in which the wing is modeled (lifting line, vortex lattice, 3-D panel arrangement, or lifting surface) because a Trefftz plane approach is used. The only conditions are a rigid wake parallel to the undisturbed flow and the oversight of the lift force acting on this rigid wake. However, according to the Trefftz plane integral, all of this comes down to modeling the lifting system as a single vortex line having the same shape as the wake trace in the Trefftz plane, and to compute the aerodynamic force resulting on this vortex line by means of the generalized Kutta-Joukowski theorem* without accounting for the self-induced velocities. Therefore in linear theory, everything acts as if all the bound vorticity were concentrated on a line and the wake extended immediately from that line. On the contrary, the following situation occurs with the 3-D wing geometries used in the Euler computations. The bulk of the bound circulation is located far forward on the wing (as for the vorticity distribution computed from thin airfoil theory on a flat plate at angle of attack) whereas the trailing vorticity is concentrated near the tip of the trailing edge. What is happening here in the Euler far field results is that

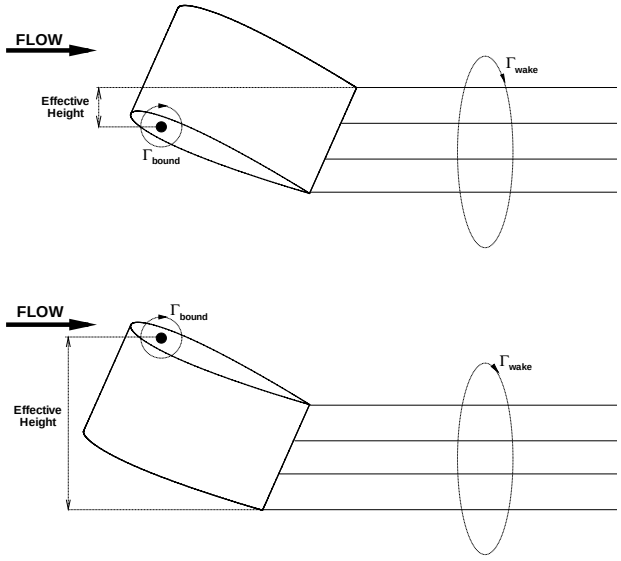


**Fig. 6** Side view of the change in effective height with wing-tips up (top) and down (bottom).

the combination of angle of attack and the layout of the bound and shed vorticity has changed the effective height of the winglet. Indeed, the most intense portion of the shed vorticity is relocated further from the bulk of the bound vorticity with downward winglets. This greater distance involves a reduction of the wake-induced downwash on the bound vortices, resulting in a drag benefit. The sketch in Fig. 6 shows the change in effective winglet height (for simplicity, the wing circulation is drawn near the quarter chord point and the wake is assumed undeformed).

Now, let us consider Eppler's results which state that induced lift makes upward winglets produce less lift-induced drag than downward ones of the same length. As it happens, the discrete Weissinger model used previously in this paper also accounts for the induced lift since both the self-induced and wake-induced velocities on the bound vortex segments are used in the aerodynamic force computation which is based on the generalized Kutta-Joukowski theorem. But, the non-linear effect of induced lift is not pointed out with this discrete model. On the contrary, it reproduces the same trends as the Euler far field results, as shown in Fig. 9 in solid line with

* $\vec{F}' = \rho(\vec{q}_\infty + \Delta\vec{q}) \times \vec{\Gamma}$

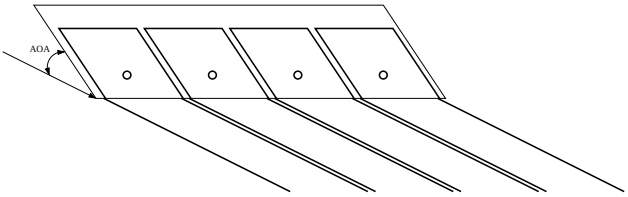


**Fig. 7** Sketch of the original discrete vortex Weissinger method.

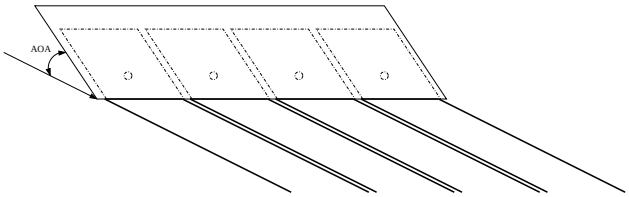


**Fig. 8** Sketch of the modified discrete vortex Weissinger method.

squares. In this discrete vortex model sketched in Fig. 7, the lifting vortices are located on the $1/4$ chord line to agree with thin airfoil theory, and a zero-normal-flow condition is enforced at collocation points at the $3/4$ chord line. However, if the lifting line is relocated at the trailing edge for the aerodynamic force computation stage (see Fig. 8), then the wake extends immediately from that line and then there is no change in effective height whether wing-tips are up or down. Therefore, the only expected effect is the induced lift. As shown in Fig. 9, this modified Weissinger method gives results in good agreement with those of Eppler, namely: winglets up produce less lift-induced drag than winglets down with the same length, and there is a minimum lift-induced drag around $\delta = 10°$ at fixed deployed span. As a consequence, the comparison of this modified Weissinger model with the original one and the Euler far field results suggests that the impact of the further layout of the bound vorticity relative to the trailing vorticity may be stronger than the effect of induced lift and overshadows the latter.

### 3.5 Remarks on the Streamline Pattern

The Spreiter and Sacks theory[11] provides a reinforcement of the Euler far field results. This

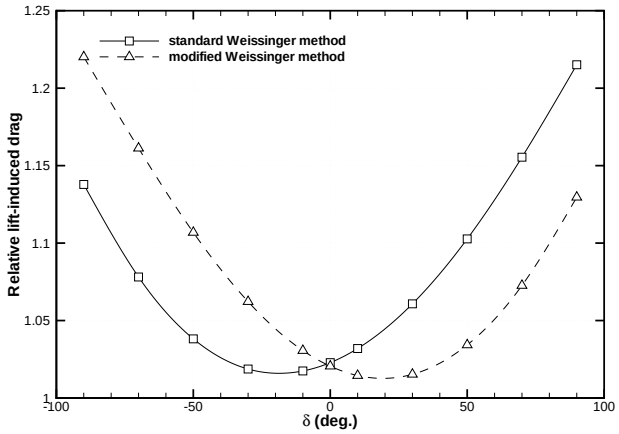


**Fig. 9** Relative lift-induced drag with the original and modified Weissinger models.

theory states that the further the wing-tip vortex core is from the wing symmetry plane, the lower lift-induced drag is. As depicted in Fig. 10, the downward wing-tip features a rolling-up significantly outer than the one observed for the upward wing-tip of the same height and span. This agrees with a lower lift-induced drag when wing-tips are folded down. Moreover, with real viscous flows there will be a separation over the upper surface when the fluid moves around the wing-tip corner from the pressure side to the suction side. This situation is sketched in Fig. 11. It is clear that this separation will involve an initial rolling-up of the vortex layer further from the wing symmetry plane in the case of downward wing-tips. This viscous effect may accentuate the difference between the two previously-depicted inviscid streamline patterns, allowing then still more lift-induced drag reduction with downward wing-tips.

## 4 Conclusion

Decades ago, the Prandtl and Munk model for lifting systems provided means to minimize lift induced drag for a great variety of wing arrangements. More recently, Eppler established a new mathematical model accounting for induced lift, a non-linear effect neglected in the Prandtl and Munk model. In the case of positive induced lift, this non-linear effect is similar to reducing the

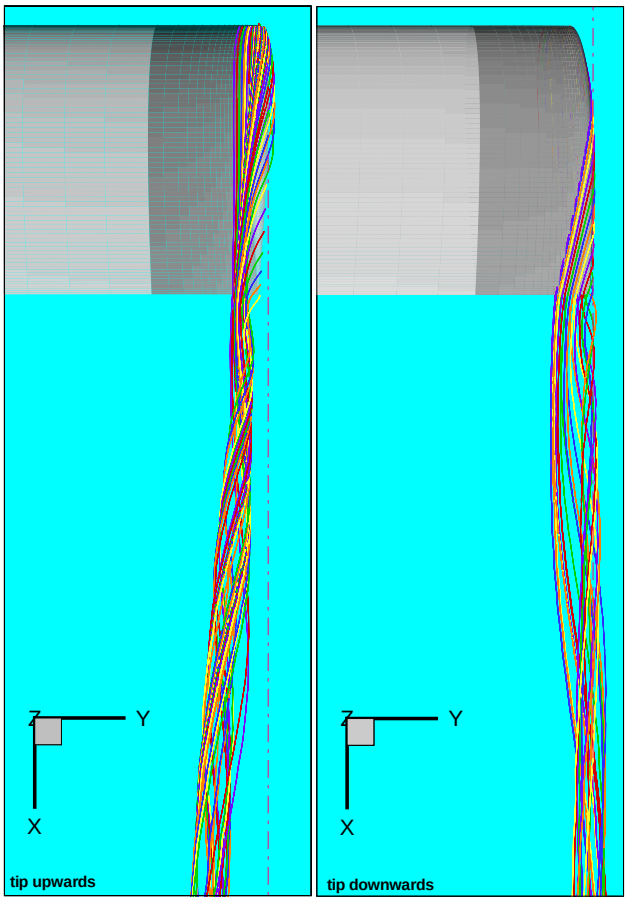


**Fig. 10** Streamline pattern at $\delta = \pm 50°$ (dash-dotted line corresponds to the spanwise tip location).

lift-induced drag for a given lift. The opposite is true for negative induced lift. It turns out with this new theory that upward winglets are more efficient than downward ones of the same length, and that the minimum lift-induced drag for a given lift and deployed span is obtained with small positive wing-tip dihedral. In the present paper, the opposite has been pointed out by using far field results of Euler numerical flow solutions. Benefits are indeed observed with downward wing-tips, which has to be ascribed to a better layout of the bound vorticity relative to the trailing vorticity. Conflicting results with Eppler indicate that the impact of this layout must be much stronger than the opposing effect of induced lift, so that it should overshadow the latter. Moreover, we may expect this situation to be strengthened in real flow because of a tip separation which would relocate the bulk

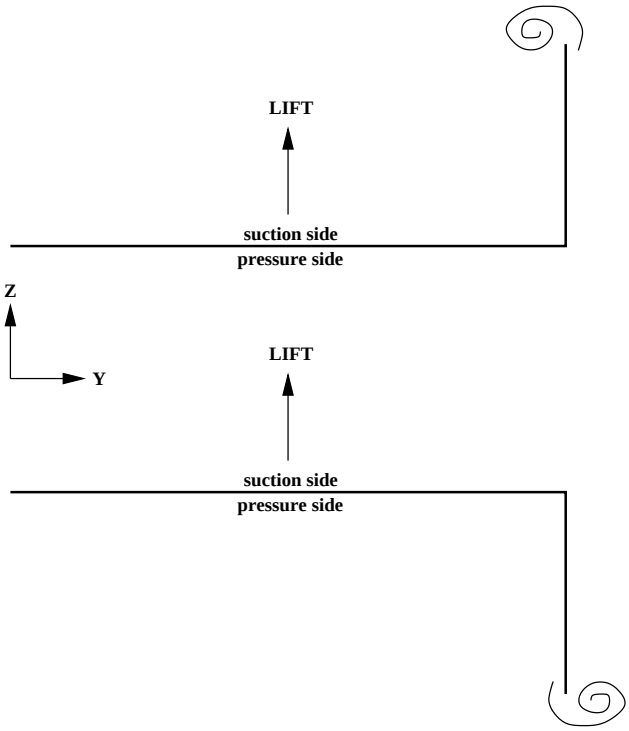


**Fig. 11** Sketch of the separation at the wing-tip for upward and downward winglets.

of the trailing vorticity further from the bulk of the bound vorticity if tips are down.

## References

[1] Cone C.D. Jr. *The Theory of Induced Lift and Minimum Induced Drag of Nonplanar Lifting Systems*. NASA TR R-139, 1962.

[2] Cummings R.M., Giles M.B., Shrinivas G.N. *Analysis of Elements of Drag in Three-Dimensional Viscous and Inviscid Flows*. AIAA Paper 96-2482, June 1996.

[3] Destarac D. *Far-Field Drag in Transonic Potential Flow: Analysis and Optimization*. European Forum, Bristol, September 1993.

[4] Eppler R. Induced Drag and Winglets. *Aerospace Science and Technology*, No 1, pp 3–15, 1997.

[5] Jameson A., Schmidt W., Turkel E. *Numerical Solutions of the Euler Equations by Finite Volume Methods Using Runge-Kutta Time Stepping Schemes*. AIAA Paper 81-1259, 1981.

[6] Munk M.M. *The Minimum Induced Drag of Aerofoils*. NACA Report No. 121, 1921.

[7] Prandtl L. *Application of Modern Hydrodynamics to Aeronautics*. NACA Report No. 116, 1921.

[8] Schmitt V., Destarac D. *Recent Progress in Drag Prediction and Reduction for Civil Transport Aircraft at ONERA*. AIAA Paper 98-0137, January 1998.

[9] Smith S.C. Private Communication.

[10] Smith S.C. *A Computational and Experimental Study of Nonlinear Aspects of Induced Drag*. NASA TR-3598, February 1996.

[11] Spreiter J.R., Sacks A.H. The Rolling-up of the Trailing Vortex Sheet and its Effect on Downwash behind Wings. *Journal of Aeronautical Sciences*, 1951.

[12] Thibert J.J. *Prévision de la Traînée à partir des Méthodes de Calcul : Etat de l'Art en France*. AGARD-AR-256, 1989.

[13] van der Vooren J., Slooff J.W. *CFD-based Drag Prediction: State of the Art, Theory, Prospects*. NLR-TP-90247-L, AIAA Technical Library, August 1990.

[14] Vanderplaats G.N. *CONMIN, a Fortran Program for Constrained Function Minimization*. NASA TM X-62, 1973.

[15] Vuillot A.M., Couaillier V., Liamis N. *3D Turbomachinery Euler and Navier-Stokes Calculation with Multidomain Cell-Centered Approach*. AIAA Paper 93-2576, June-July 1993.

[16] Zimmer H. *The Aerodynamic Optimization of Wings in the Subsonic Speed Range and the Influence of the Design of the Wing Tips*. PhD thesis, Univ. of Stuttgart, Germany, 1983.